Seismic source study of the Racha-Dzhava (Georgia) earthquake from aftershocks and broad-band teleseismic body-wave records: an example of active nappe tectonics

H. Fuenzalida, Luis Rivera, H. Haessler, D. Legrand, H. Philip, L. Dorbath, D. Mccormack, S. Arefiev, C. Langer, A. Cisternas

Geophys. J. Int. (1997) **130**, 29–46

Seismic source study of the Racha-Dzhava (Georgia) earthquake from aftershocks and broad-band teleseismic body-wave records: an example of active nappe tectonics

H. Fuenzalida,[1] L. Rivera,[1] H. Haessler,[1] D. Legrand,[1] H. Philip,[2] L. Dorbath,[1,6] D. McCormack,[3] S. Arefiev,[4] C. Langer[5] and A. Cisternas[1]

[1] *Institut de Physique du Globe de Strasbourg, 5 rue René Descartes, 67084 Strasbourg Cedex, France*
[2] *Laboratoire de Geologie Structurale, USTL. Place E. Bataillon, 34060 Montpellier Cedex, France*
[3] *Bullard Laboratories, University of Cambridge, Madingley Road, Cambridge, UK*
[4] *Institute of Physics of the Earth, Russian Academy of Sciences, Bolshaya Grunzinskaya 10, 123810, Moscow, Russia*
[5] *USGS, MS977, DCF, Denver, CO 80225, USA*
[6] *ORSTOM, 213 rue La Fayette, 75480 Paris Cedex 10, France*

Accepted 1997 February 5. Received 1997 January 2; in original form 1996 July 10

SUMMARY

The Racha-Dzhava earthquake ($Ms = 7.0$) that occurred on 1991 April 29 at 09:12:48.1 GMT in the southern border of the Great Caucasus is the biggest event ever recorded in the region, stronger than the Spitak earthquake ($Ms = 6.9$) of 1988. A field expedition to the epicentral area was organised and a temporary seismic network of 37 stations was deployed to record the aftershock activity. A very precise image of the aftershock distribution is obtained, showing an elongated cloud oriented N105°, with one branch trending N310° in the western part. The southernmost part extends over 80 km, with the depth ranging from 0 to 15 km, and dips north. The northern branch, which is about 30 km long, shows activity that ranges in depth from 5 to 15 km. The complex thrust dips northwards. A stress-tensor inversion from *P*-wave first-motion polarities shows a state of triaxial compression, with the major principal axis oriented roughly N–S, the minor principal axis being vertical. Body-waveform inversion of teleseismic seismograms was performed for the main shock, which can be divided into four subevents with a total rupture-time duration of 22 s. The most important part of the seismic moment was released by a gentle northerly dipping thrust. The model is consistent with the compressive tectonics of the region and is in agreement with the aftershock distribution and the stress tensor deduced from the aftershocks. The focal mechanisms of the three largest aftershocks were also inverted from body-wave records. The April 29th ($Ms = 6.1$) and May 5th ($Ms = 5.4$) aftershocks have thrust mechanisms on roughly E–W-oriented planes, similar to the main shock. Surprisingly, the June 15th ($Ms = 6.2$) aftershock shows a thrust fault striking N–S. This mechanism is explained by the structural control of the rupture along the east-dipping geometry of the Dzirula Massif close to the Borzhomi-Kazbeg strike-slip fault. In fact, the orientation and shape of the stress tensor produce a thrust on a N–S oriented plane. Nappe tectonics has been identified as an important feature in the Caucasus, and the source mechanism is consistent with this observation. A hidden fault is present below the nappe, and no large surface breaks were observed due to the main shock. The epicentral region is characterized by sediments that are trapped between two crystalline basements: the Dzirula Massif, which crops out south of Chiatoura, and the Caucasus Main Range north of Oni. Most, if not all, of the rupture is controlled by the thrusting of overlapping, deformed and folded sediments over the Dzirula Massif. This event is another example of blind active faults, with the distinctive feature that the fault plane dips at a gentle angle. The Racha Range is one of the surface expressions of this blind thrust, and its growth is the consequence and evidence of similar earthquakes in the past.

Key words: aftershocks, Caucasus, earthquake-source mechanism, seismotectonics.

INTRODUCTION

The epicentral region of the Racha earthquake is located on the southern slope and near the main thrust of the Western Great Caucasus (Fig. 1). Both the Great and Lesser Caucasus are under a compressive stress regime, originating from the relative convergence of the Arabian plate and the Russian platform (Philip *et al.* 1989). The deformed region is characterized by E–W-striking thrust faulting and folding, coexisting with large-scale strike-slip faulting oriented roughly $\pm 45°$ from north, and volcanic alignments that follow an approximately N–S direction (Fig. 1), implying E–W extension.

N–S shortening in the large deformed region between the Arabian plate and the Russian platform is accommodated by the lateral expulsion of the Eastern Turkish and Western Iranian blocks, while the greater part of the Great and Lesser Caucasus is involved in the frontal continental collision. Several destructive earthquakes have taken place in and around the Caucasus in the last few years, changing the prevailing ideas about the maximum size of the earthquakes in the region. The 1970 Dagestan ($Ms=6.5$) thrust earthquake took place on the northern slope of the Great Caucasus. 18 years later, the Spitak earthquake ($Ms=6.9$) occurred near the main southern thrust of the Lesser Caucasus. The 1990 Manjil (Iran) earthquake ($Ms=7.3$) took place in the easternmost part of the deformed collision wedge, near the southwestern coast of the Caspian Sea. The Manjil earthquake had a sinistral strike-slip mechanism, as expected from the lateral expulsion of the Iranian block. Finally, in 1992 another strike-slip event ($Ms=6.8$) occurred in Erzincan (Turkey) on the North Anatolian fault. Thus, the Racha-Dzhava earthquake forms part of this series of recent major earthquakes, all of them related to the continental collision (Fig. 1).

Catalogues of historical seismicity in the Caucasus led to the idea that there were no earthquakes with magnitude over 6. The exception, and a most destructive one, was the Shemakha 1668 earthquake, which affected the eastern half of the Great Caucasus. This earthquake has been the subject of a wide debate. For example, Nikonov (1982) proposed a magnitude larger than 7. On the other hand, Borisov (1982) criticised this point of view by pointing out that several historical earthquakes might have been gathered into one. Careful observation of LANDSAT images shows that the linearity of the southern border of the Great Caucasus along the Alazani basin could allow for a rupture length that might reach 100 km. The Spitak earthquake dramatically changed the belief about maximum possible earthquakes in the Caucasus. Later, the Racha earthquake reinforced this new point of view.

We may divide the Great Caucasus into two zones (Philip *et al.* 1989), east and west of the Borzhomi-Kazbeg strike-slip fault (Fig. 1). This large strike-slip fault cuts across the

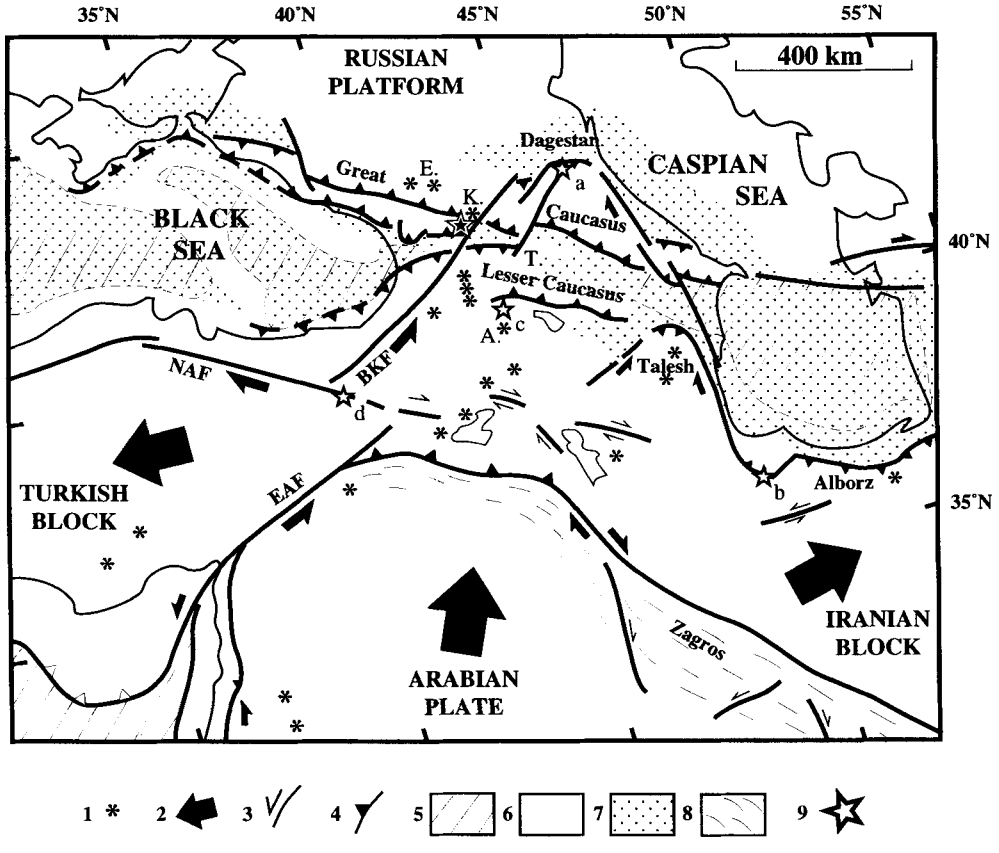

Figure 1. Present-day seismotectonic features in the area surrounding the Georgian-Ossetian earthquake, after Philip *et al.* (1989). The double star indicates the epicentre of the Racha-Dzhava earthquake and the open stars show the epicentres of (a) the Dagestan (1970), (b) the Iran (1990), (c) the Spitak (1988), and (d) the Erzincan (1992) earthquakes. (1) recent volcanoes, (2) relative motion with respect to Eurasia, (3) major strike-slip faults, (4) major thrust faults, (5) oceanic or intermediate crust, (6) continental crust, (7) main sedimentary basin, (8) recent folding at the border of the Arabian Plate, (9) epicentre of major earthquakes. K: Kazbeg volcano; E: Elbruz volcano; A: Aragat volcano; T: Tbilisis; EAF: East Anatolian Fault; NAF: North Anatolian Fault; BKF: Borzhomi-Kazbeg Fault.

mountain chain, producing a shift of the axis of the range, which also continues at depth, as shown by the gravity maps and by a twist in the Moho surface (Philip *et al.* 1989). The Borjomi Kazbeg fault may be followed towards the southwest into the North East Anatolian fault. It is characterized by spectacular left-lateral and horizontal striations found in the walls of the Kura River canyon north of Borjomi. The fault becomes more complex northwards as it enters the Great Caucasus, splitting into several branches, in particular one going along the military road next to the Kazbeg volcano, and another going through the western end of the Alazani basin. The occurrence of the Racha earthquake indicates N–S convergence west of the Borzhomi-Kazbeg fault, but is not contradictory with the jump in deformation across it. In fact, continental collision is more developed to the east of the Borzhomi-Kazbeg fault than to the west of it.

The eastern zone is characterized by extended deformation on the northern slope of the Great Caucasus east of the Borzhomi-Kazbeg fault, with the presence of important folding and reverse faulting near and around Dagestan. The northern flank of the Great Caucasus on the other hand, west of the Borzhomi-Kazbeg fault, shows a smooth monocline. Another difference is the absence of active volcanoes east of the Borzhomi-Kazbeg fault, compared with the active volcanoes to the west (e.g. Kazbeg and Elbruz). Moreover, seismic activity to the east is much more important than that to the west. Indeed, there is little historical information about great earthquakes in the Western Great Caucasus, the Racha-Dzhava being the largest known event. Finally, the Eastern Great Caucasus forms a wedge (Philip *et al.* 1989) bounded to the east by a system of right-lateral strike-slip faults, well described by Kopp (1982) and characterized by *en echelon* alignments of mud volcanoes across the eastern border of the Kura Basin, which continues further south along the southwestern border of the Caspian Sea (Fig. 1).

The Talesh minor wedge is also advancing northwards, as shown by its northern thrust front and by impressive folding ahead of the tip of the wedge, as seen in LANDSAT images. We differ in this point from the interpretation of Triep, Abers & Lerner-Lam (1995) (AR in their Fig. 1; the sense of the large arrow is inconsistent with the northern thrust and left-lateral motion on the AF).

The Racha-Dzhava earthquake of 1991 April 29 ($Ms=7.0$) is also the largest instrumentally recorded event in the Caucasian region. The Spitak earthquake of 1988 December 7 ($Ms=6.9$), located in the neighbouring republic of Armenia about 200 km south of the Racha-Dzhava epicentre, is slightly smaller. The Racha hypocentre reported by the NEIC (National Earthquake Information Center) was situated at 42.453°N, 43.673°E, at a depth of 17 km and an origin time 09:12:48.1 GMT. The event occurred on the southern slope of the Great Caucasus Range about 120 km north of Tbilisi in the Georgian Republic and partly in Southern Ossetia.

The Harvard CMT solution (PDE) was a double-couple focal mechanism corresponding to a pure thrust fault with the fault plane dipping 39°N (Fig. 2). This solution is compatible with N–S compression, in agreement with the tectonics of the Caucasus and the regional structural features (Philip *et al.* 1989).

The destruction in the Racha-Dzhava region was very great and widespread. In spite of being larger than the Spitak 1988 earthquake, the number of deaths was smaller, only 120 compared with the 25000 killed during the Spitak event (Cisternas *et al.* 1989). Much of this effect is due to the absence of large urban centres in the epicentral area of the Racha earthquake.

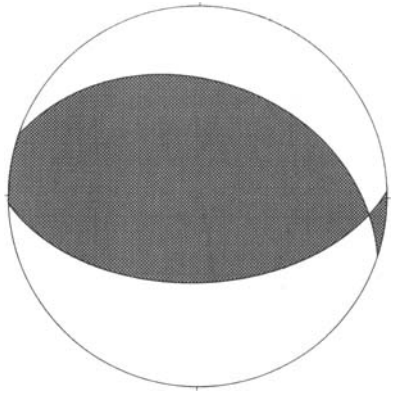

Figure 2. Best double-couple focal mechanism from the Harvard centroid moment tensor.

A seismic expedition to the area was organised some days after the event by a combined team from Moscow, Georgia, the USGS, Cambridge and Strasbourg to study the effects of the earthquake, to look for surface ruptures and to install 37 seismic stations in order to record the aftershock activity, as was done for the Spitak earthquake. Strong-motion instruments from the ETH in Zurich were also deployed around the source region in order to register aftershocks. The eastern extremity of the affected area, South Ossetia, was not accessible to us due to border problems in the region. An independent US and Russian team deployed seven instruments within the aftershock zone north of Georgia and in South Ossetia (Triep *et al.* 1995).

The main surface features observed by ourselves and others (Jibson *et al.* 1994) after the main shock were secondary ones, even though very spectacular: activation of a large number of landslides, new ground water sources and cracks on top of anticlines. Since no evidence of direct surface faulting was observed, this earthquake falls into the group of blind faults (Stein & Yeats 1989). However, this is a new kind of blind fault, because it is related to the nappe tectonics that characterize the southwestern front of the Great Caucasus (Dotduyev 1986).

In this paper we study and analyse the aftershock activity recorded from May 8 to May 31 and from June 1 to July 15. We also relocate early aftershocks between April 29 and May 8. Our information is mainly based on direct access to field information in Georgia and on seismic recordings from a dense network, which were subjected to careful checking for arrival times and polarities in order to improve the determination of hypocentres and the mechanisms of aftershocks.

Focal mechanisms are obtained for many aftershocks, and stress-tensor inversion (Rivera & Cisternas 1990) is performed. The results of the aftershock distribution from analysis of data from the local temporary seismic network and its correlation with the geology of the region are used for calculating a first

trial model for the body-wave inversion. Finally, we invert broad-band seismograms from the global network for the main shock and for the three largest aftershocks using the technique developed by Nabelek (1984). We model the source and time history of the rupture of the Racha-Dzhava earthquake and propose an interpretation for the whole sequence, that is the main shock and the aftershocks. Our results differ from those of Triep *et al.* (1995) in some aspects; this will be discussed below.

TECTONIC CONTEXT

The epicentral region of the Racha earthquake is situated just west of the Borzhomi-Kazbeg fault zone and has been carefully studied in the classic works of soviet geologists (see e.g. Milanovsky & Khain 1963; Zonenshain & LePichon 1989; other references may be found in Philip *et al.* 1989). A most important tectonic feature in the region of the earthquake is the underthrusting of the Dzirula Massif under the main range of the Great Caucasus. This thrusting takes the form of nappe tectonics that extends from the Borzhomi-Kazbeg fault zone to the Black Sea (Fig. 3). The main thrust surface around the epicentral region is a low-angle surface dipping northwards, covered by Jurassic flysch and Jurassic, Cretaceous and Tertiary sediments that were deposited in the marginal sea before collision (Philip *et al.* 1989). The flysch is strongly folded and faulted and exhibits cleavage. The more recent sediments have been subjected to folding whose intensity decreases towards the south. Thus, the Great Caucasus acted like a 'bulldozer', pushing the sedimentary wedge to the south, on top of the Dzirula Massif, which is a crystalline basement formed by the cropping out of Precambrian and lower Palaeozoic rocks.

The epicentral area of the earthquake is located to the northeast of the Racha Range, which is the anticlinal part of a fold reaching more than 2500 m in height. This range is part of the deformed sedimentary package with fold axes oriented in an approximately E–W direction. Some important geological structures surrounding the epicentral zone (Fig. 3) include the Borzhomi-Kazbeg strike-slip fault to the east, the thrusting of the Okriba-Sachkhere zone over the Dzirula Middle Massif to the south, and the Utsera fault to the north (Borissoff & Rogozhin 1993).

The field investigations carried out by ourselves and other geologists indicated that there were no primary surface ruptures caused by the main shock. All the ruptures observed were due to landslides or other forms of gravitational collapse (Borissoff & Rogozhin 1993; Jibson *et al.* 1994).

According to Borissoff & Rogozhin (1993), the available geological observations support the idea of a crystalline basement, the Dzirula Massif, dipping gently to the north. They constructed a cross-section for the region, based on geological considerations, which shows the basement surface dipping gently to the north with a depth of 5 km south of the epicentre zone and 7–10 km in the north. Finally, they noticed the existence of highly mobile serpentinized clay and gypsum loaded layers in the regional sedimentary column, which could act as parting planes for the overlying deposits.

Our block diagram (Fig. 4) is derived from previous field work in the region (Philip *et al.* 1989), from previous work by soviet geologists as indicated above and from discussions with Borisoff & Rogozhin (1993). It shows the mechanism of

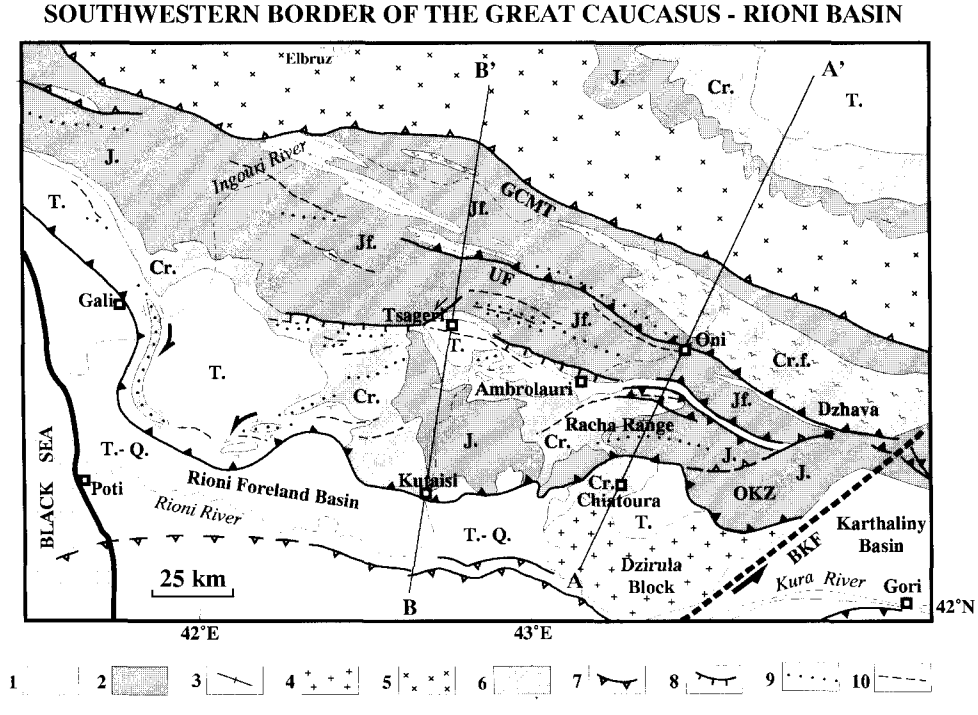

Figure 3. Main structural features around the epicentral region compiled from Philip *et al.* (1989). (1) Tertiary–Quaternary sediments, (2) deformed Jurassic sediments, (3) metamorphic basement, (4) crystalline basement—Dzirula Massif, (5) crystalline basement of the Great Caucasus Main Range, (6) Cretaceous sediments, (7) thrusts, (8) normal faults, (9) anticlines, (10) synclines. T-Q: Tertiary–Quaternary; T: Tertiary; Cr: Cretaceous; Cr.f: Cretaceous flysch with schists; J: Jurassic; Jf: Jurassic flysch with schists; BKF: Borzhomi-Kazbeg Fault; OKZ: Okriba-Sachkere zone; UF: Utsera fault; GCMT: Great Caucasus Main Thrust.

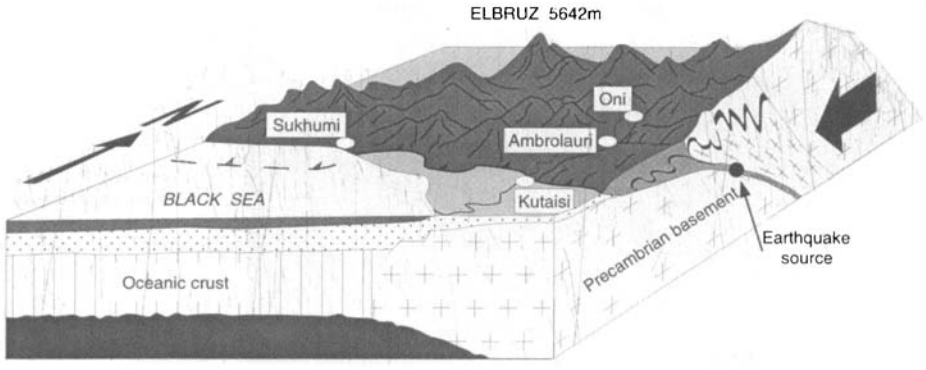

Figure 4. Geological block diagram of the region showing the collision, overthrusting to the south, folding and faulting of nappes over the basement rocks (Dzirula Massif).

collision of the Arabian plate and the Russian platform with a sedimentary wedge being squeezed between the crystalline basement of the Great Caucasus and the Dzirula Massif. It also shows the flat subhorizontal deformed sedimentary package that defines the nappe 'decollement' and the fracturing in the crystalline basement. The nappe is much more developed to the west than to the east. Our interpretation differs from that of Borisoff & Rogozhin (1993) only in the assumption that the fracturing of the Dzirula crystalline massif existed before the initial stages of collision, namely during the extension period associated with the old marginal sea that joined the Black and Caspian seas (Philip *et al.* 1989). The earthquake suggests that this nappe is active and that it can be considered as the eastern continuation (Fig. 3) of the nappe tectonics observed between the Ingouri and Rioni rivers (Philip *et al.* 1989). The main rupture, as we will show below, is not related to fracturing within the Dzirula block, but to the advance of the sedimentary wedge on top of it.

TEMPORARY SEISMIC NETWORK

Ten days after the earthquake a multinational temporary seismic network was installed in the epicentral area to complement the near-source coverage of the permanent Georgian regional network, which had three stations near the epicentral region. The field experiment can be divided into two periods. The first was from May 9 to the first days of June, when the temporary network was fully operational, with 37 stations and a close time control. During this time, readings and checks were made by the Strasbourg team. During the second period, from June until August, the network continued to function, but readings were made separately by each group and gathered together afterwards. The temporary network consisted of three types of instruments (Fig. 5 and Table 1):

Analogue stations

12 sites were occupied by smoked-paper recorders (Sprengnether MEQ-800) equipped with one-component vertical seismometers (Mark-Product L4C, $T_o = 1$ s). The amplifications ranged from 72 to 84 dB according to local background noise. The drum speed was set to 1 mm s^{-1}, allowing for 48 hr of continuous operation. Time marks were recorded every second, allowing us a precision of 0.05 s in the readings of *P*-wave arrivals. The seismographs included temperature-compensated crystal clocks whose drift was controlled by the Moscow Radio time signals every 48 hr during the entire experiment. This allowed us to correct the timing of phase readings.

Digital stations

Six sites had Geostras (Institut de Physique du Globe de Strasbourg) digital recorders equipped with three-component seismometers (Mark Product L22, $T_o = 0.5$ s). The signals were sampled at a rate of 150 samples per second with dynamics of 72 dB plus 18 dB used for the automatic gain range. The recording process was triggered by an STA/LTA-type algorithm. Time signals were obtained from the worldwide Omega system emitting from Norway. 10 additional single-component digital recording stations (DSR), built in Cambridge, were installed by the Cambridge group (McCormack 1994).

Telemetric stations

Nine stations belonging to the Strasbourg telemetric network were linked via FM radio; eight of them at remote sites were equipped with one-component vertical seismometers (Mark Product L4C, To = 1 s) and the central receiving site was equipped with a three-component seismometer (Mark Product L4–3D, $T_o = 1$ s). The internal clock at the central site was recorded simultaneously with DCF (radio transmitter in Germany) and Omega time signals. Seismic and time signals were digitized at a rate of 75 samples per second and then recorded on digital audio tape (DAT). Recording was triggered when a pre-set number of stations (typically four) received a signal which exceeded a selected threshold within a given time window.

The whole network covers most of the aftershock area but access was not possible in South Ossetia, due to political problems at the border. Therefore, in order to locate the most important events on the eastern side, readings from the closest stations of the regional network (ZEI and GOR) were incorporated. Special care was taken to include station corrections with respect to the velocity model. These time delays were calculated by selecting the best-located events and then taking the average value of the residuals at each station.

AFTERSHOCK DATA ANALYSIS

All *P* and *S* arrival times for each station were read from May 9 to May 31. These readings were combined afterwards

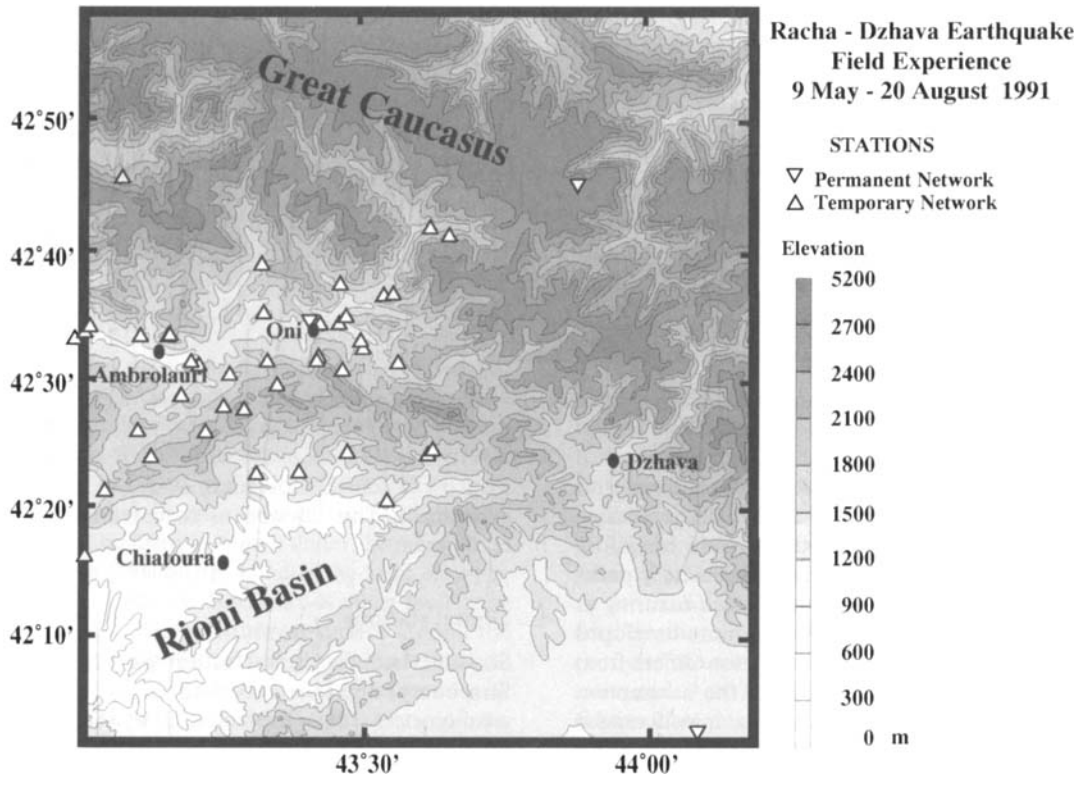

Figure 5. Distribution of stations of the temporary network (open triangles) and some Georgian permanent stations (inverted open triangles). The Racha Range is the long, E–W oriented arc-like feature west of Dzhava.

and regrouped by event. 1940 aftershocks were thus identified and located for this period. A simple velocity model, consisting of a layer 4 km thick with a P velocity $V_p = 5.3$ km s^{-1}, over a half-space with $V_p = 6.0$ km s^{-1}, was used for locating the hypocentres. This is the same model as used for locating the Spitak aftershocks (Dorbath *et al.* 1992).

Aftershock hypocentres were determined by using the HYPO71 algorithm (Lee & Lahr 1975). A selection of events based on the quality of the solutions was made. All events with hypocentre quality Q = A, B or C and with at least one S reading were retained. The parameter Q is an output of HYPO71 that gives information about the quality of the locations obtained. The quality classes, Q = A, B or C, correspond roughly to RMS < 0.5 s; ERH < 5.0 km; number of phases weighted in solution ≥ 6 and GAP $\leq 180°$ (Lee & Lahr 1975). 966 events fulfilled these criteria. Fig. 6 shows the distribution of hypocentre location error outputs in order to illustrate the quality of the solutions, together with the depth distribution for the above 966 aftershocks.

P-wave polarities were read at the same time as P and S arrival times. These data were used as input in the stress-tensor inversion algorithm developed by Rivera & Cisternas (1990). The output consists of a unique stress deviator orientation and shape, and the compatible individual focal mechanisms that are consistent with the observed polarities for each event.

The early strong aftershocks that occurred before the installation of the temporary network were recorded by the Georgian network alone. These events were relocated after using station corrections for the Georgian stations (Fig. 16). The station corrections were obtained from aftershocks that were accurately located by the temporary network and were simultaneously recorded by the Georgian stations as described above. All events with quality A or B were used. This set of events permitted the calculation of theoretical traveltimes to the Georgian permanent network and the establishment of station corrections for 10 of them. The epicentres were relocated using the HYPO71 routine with fixed depths, since the S phase readings were not reliable at these epicentral distances.

Aftershock distribution and stress tensor

The Georgian catalogue of seismicity (Gorshkov 1984) for the period 1962–1988 shows some sparse activity around the Racha Range, though some of it may be due to the presence of several quarries. Thus, a period of quiescence preceded the Racha earthquake.

The aftershock distribution (Fig. 7a) forms an elongated cloud trending N110°–120°, more than 80 km long and 20 km wide, extending from Ambrolauri to Dzhava. It is wider on the western half and it narrows towards the eastern end. It is observed that the eastern part presents a more diffuse character, probably due to the network geometry (in particular the absence of stations in South Ossetia). In contrast, the western part defines relatively well two elongated clusters that surround a zone with almost no aftershock activity. A clear correlation with topography is observed (Figs 5 and 7a). The southern cloud of aftershocks runs parallel and slightly south of the crest of the Racha Range for a distance of 60 km. Depths range from 2 to 15 km. The western extremity of this aftershock cloud shows a change in direction, turning to the north at the point where the Racha Range changes trend in the opposite

Table 1. Geographical coordinates and station types of the temporary network used in determining the aftershock hypocentres.

Station Code	Latitude	Longitude	Elevation (m)	Type
gON2	42°34.37′N	43°26.18′E	790	Georgian
dSBI	42°33.32′N	43°06.34′E	603	DSR
dKHA	42°25.13′N	43°02.81′E	1130	DSR
dDZE	42°14.37′N	42°56.68′E	234	DSR
dKVR	42°23.28′N	43°27.16′E	570	DSR
dHOH	42°23.09′N	43°36.54′E	888	DSR
dSIN	42°23.50′N	43°37.11′E	978	DSR
dSAM	42°33.12′N	42°55.50′E	421	DSR
dSKD	42°37.81′N	43°26.31′E	1070	DSR
dSEV	42°31.55′N	43°23.79′E	1260	DSR
dIRD	42°31.01′N	43°33.05′E	1128	DSR
spe	42°19.12′N	43°31.79′E	711	GEOSTRAS
mok	42°21.58′N	43°21.55′E	465	GEOSTRAS
tsi	42°21.43′N	43°16.58′E	850	GEOSTRAS
kve	42°23.29′N	43°27.17′E	515	GEOSTRAS
shk	42°27.23′N	43°12.77′E	1291	GEOSTRAS
sak	42°37.81′N	43°26.31′E	1070	GEOSTRAS
gar	42°36.85′N	43°31.38′E	990	MEQ
sor	42°35.31′N	43°17.41′E	715	MEQ
zem	42°31.13′N	43°17.84′E	1270	MEQ
nig	42°34.36′N	43°23.97′E	760	MEQ
sho	42°42.67′N	43°36.77′E	1349	MEQ
bok	42°31.19′N	43°23.60′E	1333	MEQ
sad	42°33.41′N	43°06.53′E	640	MEQ
ckv	42°33.66′N	42°56.66′E	500	MEQ
sva	42°30.01′N	43°13.47′E	1020	MEQ
tsk	42°32.25′N	43°28.97′E	1235	MEQ
hot	42°28.20′N	43°07.81′E	1020	MEQ
cha	42°28.18′N	43°07.86′E	1000	MEQ
ts2	42°32.90′N	43°28.70′E	1120	MEQ
amz0	42°30.79′N	43°09.92′E	838	TELEMETRE
amn0	42°30.79′N	43°09.92′E	838	TELEMETRE
ame0	42°30.79′N	43°09.92′E	838	TELEMETRE
gom1	42°36.94′N	43°32.48′E	1360	TELEMETRE
joc2	42°34.17′N	42°57.26′E	686	TELEMETRE
ura3	42°39.52′N	43°17.19′E	1271	TELEMETRE
tki4	42°22.90′N	43°04.35′E	1610	TELEMETRE
sat5	42°25.04′N	43°10.67′E	1724	TELEMETRE
pyt6	42°29.10′N	43°18.98′E	1900	TELEMETRE
tch7	42°33.32′N	43°03.13′E	732	TELEMETRE
uch9	42°30.38′N	43°26.59′E	2422	TELEMETRE
UCH9	42°26.98′N	43°15.15′E	1177	TELEMETRE

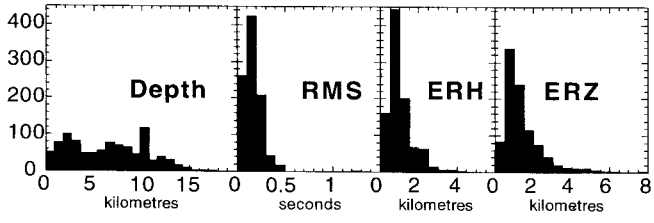

Figure 6. Histograms of depth, rms arrival-time mean error, epicentral error, ERH, and depth error, ERZ, for the selected 966 events (1991 May 9–31).

direction (Fig. 7a). The cloud is not continuous, and some clusters may be identified. The topography of the Racha Range is segmented and individual topographic heights coincide with the aftershock clusters. An E–W cross-section through the seismicity cloud (Fig. 7b) indicates an increase in depth towards the east. Transverse cross-sections (Fig. 7b) show that seismicity dips to the north at about 30°. The northern cloud of aftershocks is situated below the Oni Valley, which runs parallel to the Great Caucasus. Depths range from 5 to 15 km within this cloud.

As mentioned above, an interesting feature observed on the western part of the aftershock distribution is the almost complete absence of activity between the two branches of aftershocks. Two alternative explanations are possible for this feature. The first possibility, and the one that we favour, is that this gap may be thought of as a part of the main rupture surface, where the stresses have been almost completely relaxed, and consequently few aftershocks may occur later on [Triep *et al.* (1995) also give the argument of excess overburden]. In this scenario the two branches are part of the same fault surface, that is they are connected through the region of weak activity. Cross-sections AA′ and BB′ in Fig. 7(b) show the transition to a continuous surface as we move east along the aftershock cloud. The second possibility is that the two elongated clouds could be viewed as two independent, nearly parallel fault breaks. Consequently, in this case it is not possible

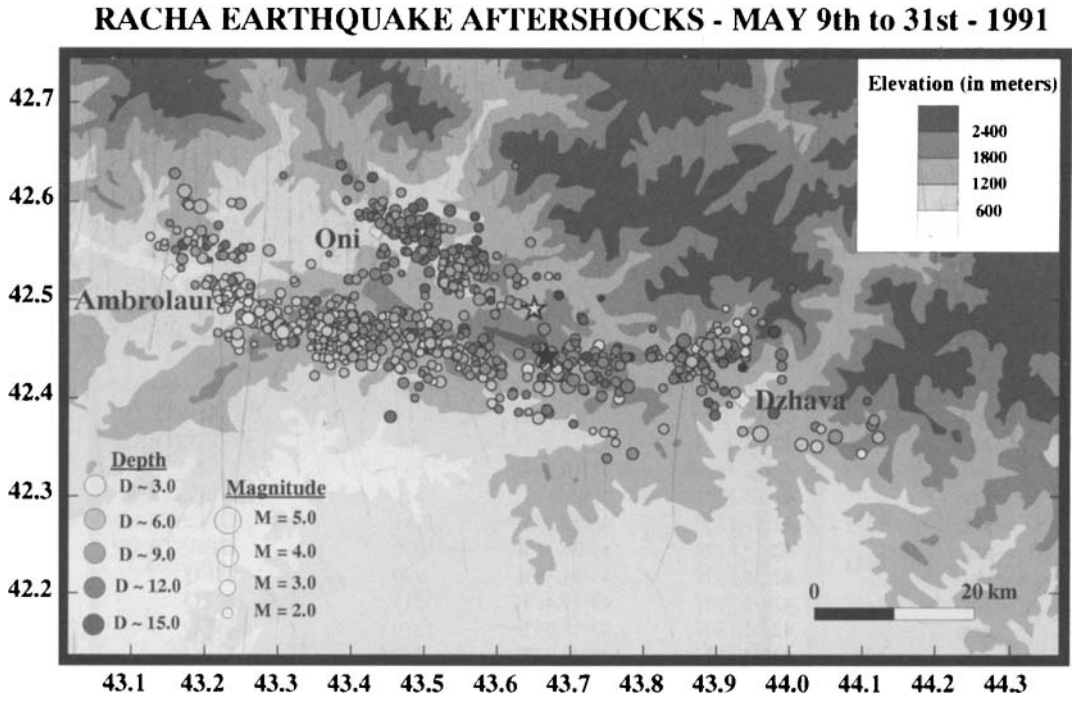

Figure 7. (a) Aftershock distribution of the Racha-Dzhava earthquake. The solid star shows the location of the NEIC epicentre and the open star is the location of the Harvard CMT centroid. Events have an epicentre quality A, B or C and rms value <0.5 s. (b) Cross-sections of the aftershock distribution showing the north-dipping activity and depth confinement for the southwestern activity between 2 and 7 km and 7–13 km for the northern branch, and an E–W cross-section of the southernmost aftershocks. (c) Aftershock distribution for June and the first few days of July.

to define the geometry of the main shock based on the aftershock distribution alone, and additional independent information is necessary to solve this problem. Triep *et al.* (1995) add as a third possibility that '*...the fault lies completely* in the basement...'. We believe that this third case is unlikely because the long-term earthquake process is related to shortening and folding of the sedimentary wedge through decollement. ' The aftershock activity during the following period, that beginning in June and ending in August at the end of the field experiment (Fig. 7c), is roughly the same. The aftershock distribution is more scattered because of the reduction in the number of stations and the loss of accuracy in phase readings. The only significant difference arises from the swarm of activity triggered around the strong aftershock of June 15 ($Ms=6.2$) (Figs 7a and c). This activity implies fault growth to the east of the main shock. McCormack (1994) studied this sequence in detail and showed that no clear geometry can be established from the aftershock distribution, because of the uncertainties resulting from the absence of stations towards the southeast.

The aftershock sequence shows a complete absence of activity under the western part of the range, south of Ambrolauri, which suggests to us decoupling and segmentation in the mechanism of range building between the eastern part of the fold, which was activated during the earthquake, and its western part, trending WSW, which was not activated.

Triep *et al.* (1995) produced a roughly similar epicentre distribution. They used seven stations within the aftershock cloud and three outside, which worked over variable periods of time (their Table 1) but mostly from May 15 to June 6. They complemented their data with a first version of our data set for the period May 7 to June 30. As a result, they obtain good depth control for aftershocks within Ossetia for the events within the period of better station coverage. On the other hand, working with a carefully revised data set for the period May 9 to May 31, and then from June 1 to June 15, we had very good depth control for events within Georgia. Furthermore, we could use the polarities of first arrivals to compute focal mechanisms with our dense network.

The result given by the stress-tensor inversion is a triaxial compression tensor with σ_1 horizontal and oriented N200°, and σ_3 vertical (Fig. 8). The focal mechanisms show a large variety, and thus the stress-tensor axis directions are very well constrained. This tensor explains 89 per cent of the polarities with a likelihood of 93.8 per cent. It can be observed that the mechanisms are mostly of reverse type, with some strike-slip (Fig. 9). The tensor is in agreement with the compression character of all the structures in the region and, in general, with the convergence between Arabia and the Russian platform. The solution obtained for the Spitak aftershocks is very similar (Dorbath *et al.* 1992). Nevertheless, a 35° clockwise rotation in the azimuth of σ_1 exists between the stress tensors observed for the Spitak and Racha earthquakes. This rotation of the orientation of the maximum compressive stress axis is also observed from microtectonic measurements and has been associated with the passage from one side to the other of the Borzhomi-Kazbeg fault zone (Philip *et al.* 1989).

The strongest aftershocks recorded by the permanent network immediately after the main shock, from April 29 to May 9, show the same general features as the later activity located with the temporary network (Fig. 18), thus confirming that the aftershock area is neither overestimated nor underestimated. The location of the epicentre of the main shock with respect to the aftershock cloud also suggests a bilateral propagation of the rupture, but with a dominant segment to the west.

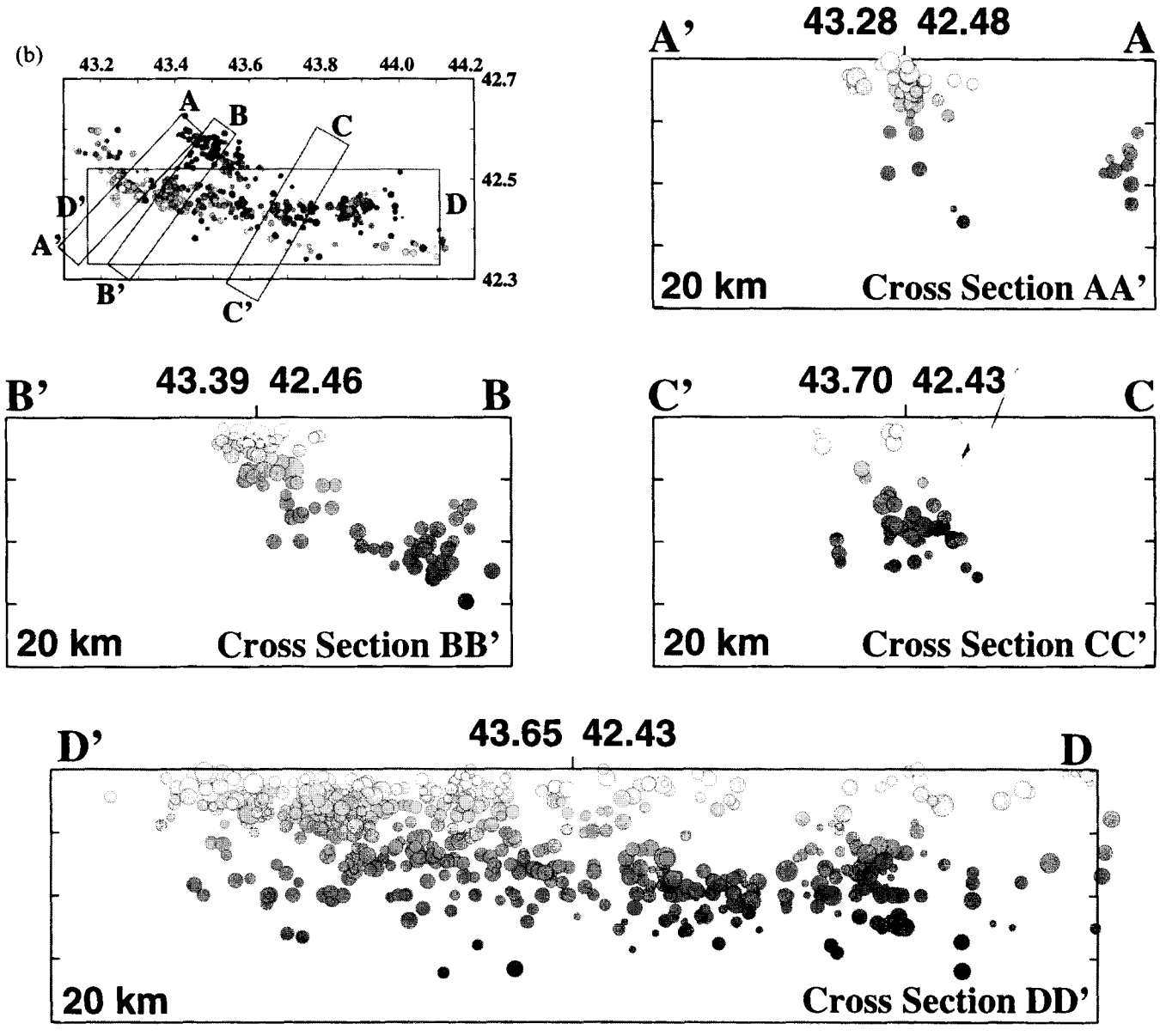

Figure 7. (*Continued.*)

BODY-WAVEFORM DATA

Broad-band (BRB) and very-broad-band (VBB) records from 16 GDSN and GEOSCOPE stations, well distributed in azimuth around the epicentre (Fig. 10), were used. Only stations within a distance range between 30° and 90° from the epicentre were selected. The crustal structure adopted in the computation of synthetic seismograms was taken to be similar to that of the Spitak region (Haessler *et al.* 1992) and that used in the aftershock location (Table 2). Displacement records were chosen for the inversion rather than the velocity records (which enhance high frequencies) in order to reduce the effect of local structure.

Inversion procedure and results

The inversion of focal parameters was performed using the algorithm of Nabelek (1984) with the choices described in Fuenzalida *et al.* (1997). The crustal structure at the stations was assumed to be a layered medium with a 4 km thick layer with a *P*-wave velocity of 5.3 km s^{-1} over a 12 km thick layer with a *P*-wave velocity of 6.0 km s^{-1}, a Poisson ratio equal to 0.25 and a density of 2.75 g cm^{-3} (Table 2).

In a first stage, we inverted 30 s of the signals looking for a single point-source model, in the same way as Triep *et al.* (1995). The solution consisted of a north-dipping thrust (strike = 293°, dip = 27°, rake = 101°) with a centroid depth of 3.8 km and a seismic moment $M_o = 2.86 \times 10^{26}$ dyne cm. This solution, although correctly resolved, does not fit the records at stations to the south and west of the source well, as indicated by arrows in Fig. 11.

In a second stage, inversion of the source time function was performed for each single station, assuming the source mechanism to be the Harvard CMT best double couple. This is equivalent to carrying out point source deconvolution (Kikuchi & Kanamori 1982; Bezzeghoud & Madariaga 1986) in order

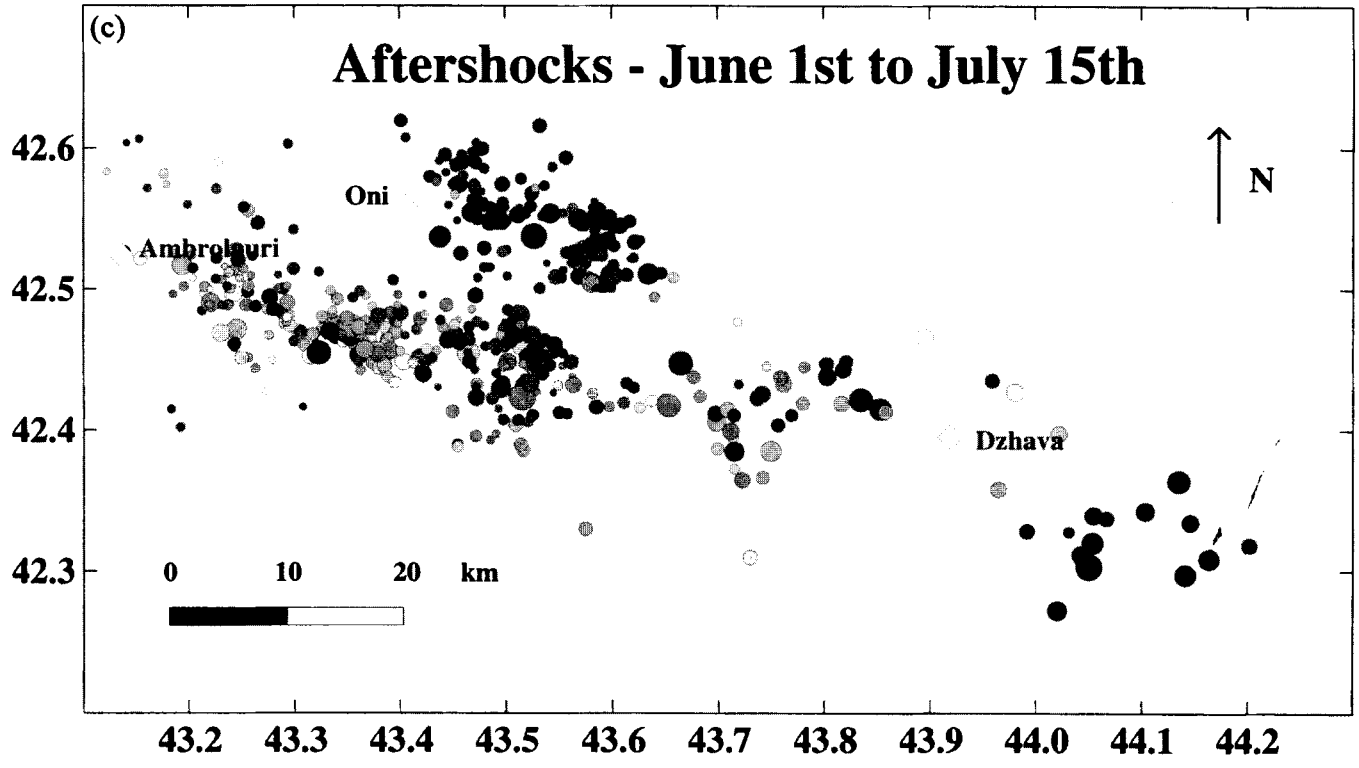

Figure 7. (*Continued.*)

to search for azimuthal dependence of the source time function, and hence facilitates the identification of subevents. The single-station source time functions (Fig. 12) present two or three peaks for stations situated to the south of the source, while a single broad peak is observed to the north. This observation led us to introduce the *a priori* knowledge of the geometry of the aftershock distribution in order to simulate a more complex source composed of additional subevents separated from the epicentre of the main shock. The shallow character of the point source was confirmed by testing the centroid depth of the inversion, which was well constrained at about 5 km (Fig. 13a).

Next, a directivity effect resulting from the propagation of the rupture was introduced in the source time function and testing was made for different rupture velocities along the strike of the plane of rupture. The misfit problems were still present. A rms minimum was found for rupture velocities between 0 and 1 km s^{-1} (Fig. 13b), which is a very low value for rupture propagation. It does not allow us to determine a sense of rupture, but suggests instead an unbalanced bilateral rupture.

The single point-source solution shows misfits in the first onset of the *P* waves, suggesting the presence of a foreshock some seconds before the main moment release. This foreshock is confirmed by the ISC bulletin, where an event is identified about 3 s before the main shock (ISC Bulletin 1993). The fit, particularly at stations to the south of the epicentral region, is greatly improved once this foreshock is introduced (Figs 11 and 14). The mechanism of the foreshock is similar to that of the main shock (Table 3 and Fig. 16), but the dip is slightly steeper at 48° rather than 29°. Its epicentre is about 3 km northwest of the main shock.

The source time function at the stations to the south exhibits two or three peaks (Fig. 12). The misfit in this interval, particularly clear for southern stations, is still present after the introduction of the foreshock and it must therefore correspond to the spatial extension of the source. Hence, a third subevent was introduced to the northwest in order to improve the fit at the southern stations (Table 3 and Figs 14 and 17). A depth of 10 km was obtained, in agreement with the hypocentres of the aftershocks in this area, and its mechanism is reverse faulting dipping 59°N. A fourth subevent was introduced 20 km to the west of the main subevent in order to complete the adjustment, and the inversion gave a strike-slip mechanism (Table 3 and Fig. 16). The contribution of this last event to the waveform modelling is shown for some selected stations in Fig. 14. We can see that it is clearer at the stations in eastern China.

The final solution therefore consists of the contributions of four sources: a foreshock; the main shock 3 s later; a subevent to the northwest 10 s later; and finally a subevent to the west 14 s later. The locations of the subevents were constrained to be within the aftershock cloud. The solutions, together with their associated errors, are summarized in Table 3. Fig. 15 shows how the synthetic *P* and *SH* waveforms fit the data. The source time function of the third subevent is superposed with that of the second (main shock) subevent (Fig. 15), and its mechanism is also reverse faulting. Nevertheless, this third subevent can be separated from the second subevent in the records of different stations, since there is an azimuth-dependent phase shift due to the separation of the sources in space (20 km). The residual misfits at each station can be interpreted as the combined effects of local structural heterogeneities at receiver sites and at the source.

The main shock represents 72 per cent of the scalar seismic moment released during the earthquake. A striking feature is

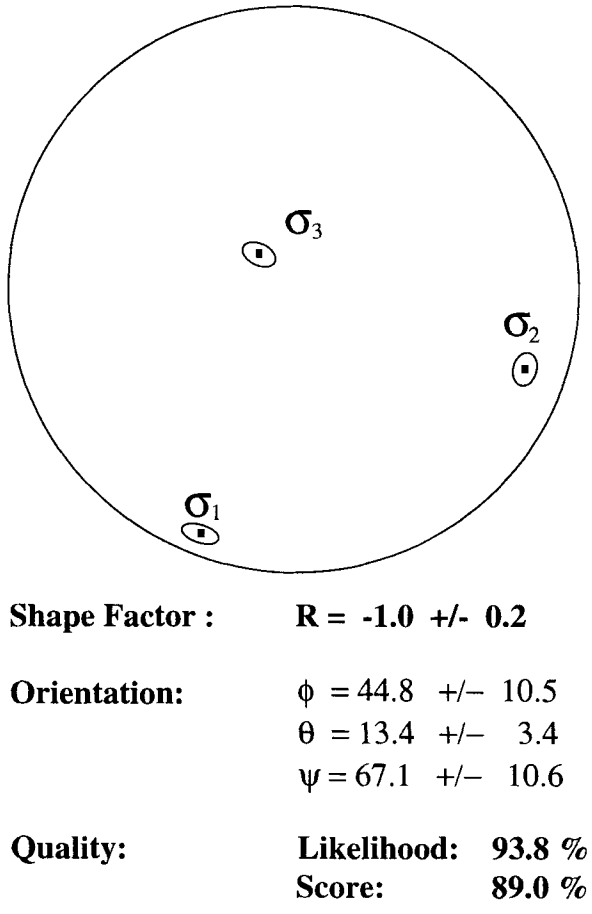

Figure 8. Stress tensor solution from *P*-wave first-motion polarity inversion. The shape factor $R=(\sigma_z-\sigma_x)/(\sigma_y-\sigma_x)$ is negative when the state of stress is in compression (the case for which σ_3 is almost vertical, $\sigma_3=\sigma_z$). The Euler angles ϕ, θ and ψ define the orientations of the principal axes of stress. One standard deviation ellipses are shown.

that most of the rupture occurred on a 29° dipping thrust. The rupture due to the main shock is limited by subevents 3 and 4 to the west, and could not extend further than the epicentre of the aftershock of April 29 ($Ms=6.1$) to the east. The aftershock cloud extends beyond the main rupture but it is more developed to the east (Fig. 16). Later aftershocks east of the April 29 event, in particular that of June 15 ($Ms=6.2$), may be interpreted as evidence of eastward fault growth, as discussed above (Fig. 16).

An alternative source-modelling scheme, that of Triep *et al.* (1995), consists of a simple rupture geometry within the eastern part of the main aftershock cluster (I in their Fig. 12), but it does not include the details of the space distribution of the rupture as indicated by the aftershocks. It coincides overall and it is compatible with a shallow thrust.

Inversion of body waveforms for the three most important aftershocks was also performed. The April 29 ($Ms=6.1$), May 3 ($Ms=5.4$) and June 15 ($Ms=6.2$) events are located towards the extremities of the aftershock cloud (Fig. 16). Inversion was performed for a single point source for each event, given their moderate size and simple waveforms. The results are shown in Table 4. They are similar to those obtained by Harvard and Triep *et al.* (1995). The June 15 aftershock corresponds to a thrust on a nearly N–S-oriented fault strike. This latter result might seem paradoxical since the main regional compression direction is roughly N–S. We will show below that this apparent discrepancy can be understood using the stress tensor.

INTERPRETATION AND DISCUSSION

The rupture was asymmetrical since there was no need to include another source to the east of the epicentre of the main shock, whereas the third and fourth subevents were located to the west of it. We observe, as for the Spitak 1988 event, that the signals begin gently on most of the seismograms, suggesting the existence of a foreshock. The Harvard centroid moment tensor with a double-couple solution, and the solution given by Triep *et al.* (1995) are similar to the one determined here, and the same is true of the total moment release.

All the results and features described previously, aftershock distribution, source of the main event, tectonic setting and focal mechanisms, suggest a complex source system. The Racha-Dzhava earthquake was produced by the overthrusting of the folded and deformed Cretaceous–Jurassic flysch and sediments over the Dzirula Massif along a gently dipping surface. It can be viewed as the result of the motion of the sedimentary wedge, which was deformed and pushed southwards by the main range of the Great Caucasus over the Dzirula Massif (Fig. 4). The shallow depth of the main centroid and the shallow depth distribution of the aftershocks are evidence in favour of nappe tectonics. The aftershock distribution with depth shows that the activity is constrained to the upper 13 km of the crust. The low-angle thrust deduced from the body-wave inversion represents roughly the decollement surface of the nappe. Borisoff & Rogozhin (1993) argued that this surface should not be understood necessarily as the exact interface between the deformed sediments and the crystalline basement, because it could alternatively be a thin layer with highly serpentinized clay or gypsum within the sedimentary cover. Nevertheless, such a hypothetical surface would not be too far from the crystalline basement.

We suggest that faulting is determined by the contrast in rheological properties between the crystalline basement and the sedimentary layers. The instability may initiate somewhere along the basement–cover discordance, at the junction between adjacent segments of the fault, and propagate upwards and laterally (Ramsay 1982). Fracturing and folding are likely to occur within the sedimentary material with a lower stress threshold, and thus are not likely to appear within the crystalline basement, which is stronger. Furthermore, we should expect the aftershock activity to be confined inside the wedge of deformed sediments and flysch. In the case where the basement is involved, we would expect to have a well-defined fault plane from the aftershock sequence. On the contrary, even though only the best-located ones have been retained, we observe that the aftershocks are rather scattered.

The aftershocks are located on the borders of the faulted region and surround a zone with almost no activity. This is particularly true for the western part since it is at this extremity that the nappe is better developed. The eastern extremity of the aftershock cloud coincides with the place where the nappe dies out. This is probably connected to the junction of the

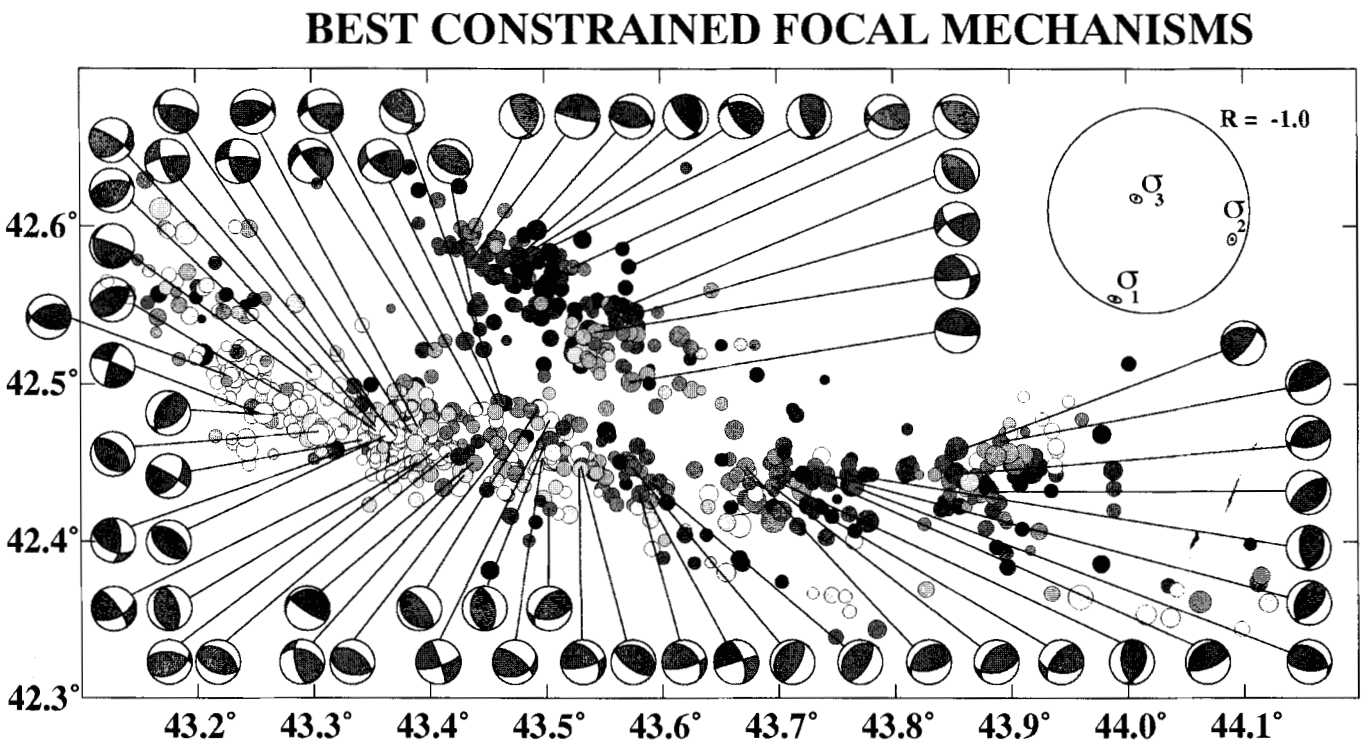

Figure 9. Stress tensors and the best-constrained focal mechanism solutions for the aftershocks.

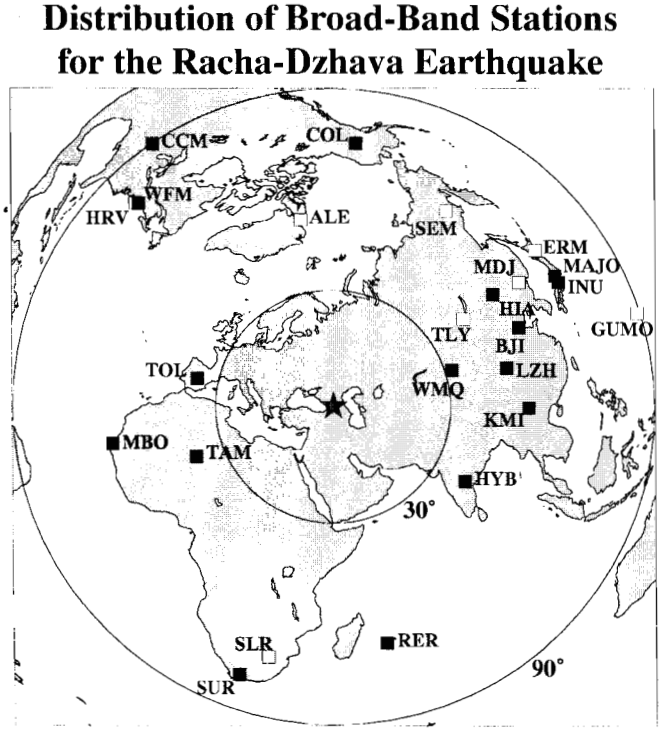

Figure 10. Geographical distribution of the teleseismic stations used in the present study showing a very good azimuthal coverage of the source region. The star indicates the epicentre of the Racha-Dzhava earthquake and the concentric circles represent 30° and 90° epicentral distance. Solid squares are stations available for the main-shock source study and open symbols are other stations used in the study of the aftershock sources.

Table 2. Crustal structure used in the hypocentre location and adopted to compute the synthetic seismograms in the body-wave inversion scheme.

Layer #	Thickness (km)	V_p (km s^{-1})	σ	Density (g cm^{-3})
1	4.0	5.3	0.25	2.60
2	12.0	6.0	0.25	2.71
3	25.0	7.3	0.25	2.85

main thrust under the Great Caucasus with the Borzhomi-Kazbeg fault (Fig. 18). We propose that the western part of the fault surface is a subhorizontal plane between the two linear clusters of aftershocks, widening from east to west, in order to approach the nappe geometry. The reason why no aftershocks are observed within this surface may be understood by looking at the stress tensor. For a very gently dipping fault plane, the minimum principal axis of the stress tensor (σ_3) is almost normal to the plane, so that the other two axes are contained within the plane, and therefore the fault is not very likely to be activated. Of course, this argument relies on the hypothesis that all pre-existing planes have a subhorizontal orientation.

The aftershocks can be gathered into four groups. The first group is on the southern branch trending E–W and situated between the fourth subevent and the aftershock of April 29 (Fig. 16). This shallow activity represents a reverse fault, along which a block of sediments is uplifted, but the dislocation along the rupture surface dies out under the southern flank of the Racha Range without arriving at the free surface. The second group is the northern branch under the Oni Valley. This deeper activity corresponds to the place where the basement–cover interface begins to dip at a steeper angle. The third group is the activity to the west of the fourth subevent, where the trend of the seismicity turns to the north, instead of continuing along the Racha Range. This effect is probably due

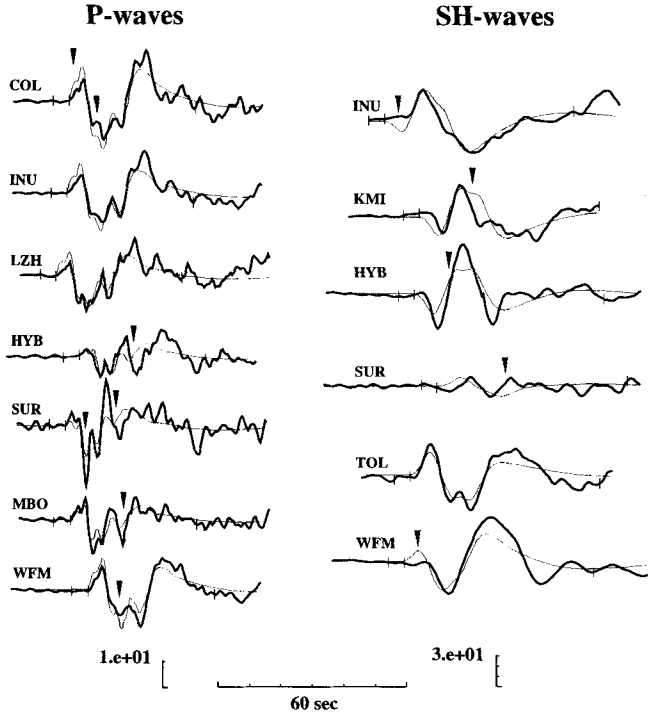

Figure 11. Comparison between observed and synthetic signals for *P* and *SH* waves from a single point-source inversion at some stations. The observed signal is shown by the heavy trace and the synthetic signal by the thin trace. The vertical bars delimit the inversion window of each seismogram. The arrows indicate misfits. The scales are different for *P* and *SH* amplitudes.

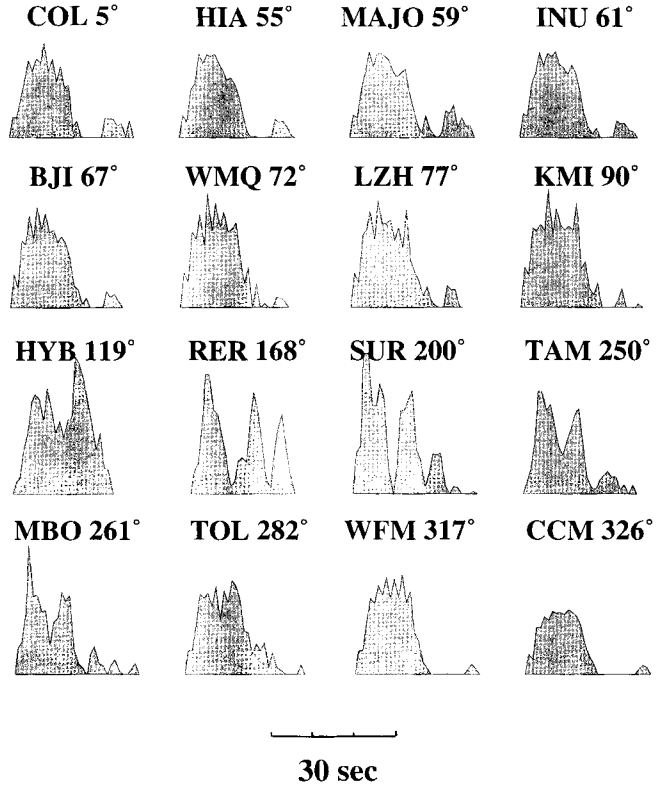

Figure 12. Point-source deconvolution from *P* waves for different stations showing splitting of the pulse for signals recorded to the south of the epicentral region. Delays are between 7 and 10 s.

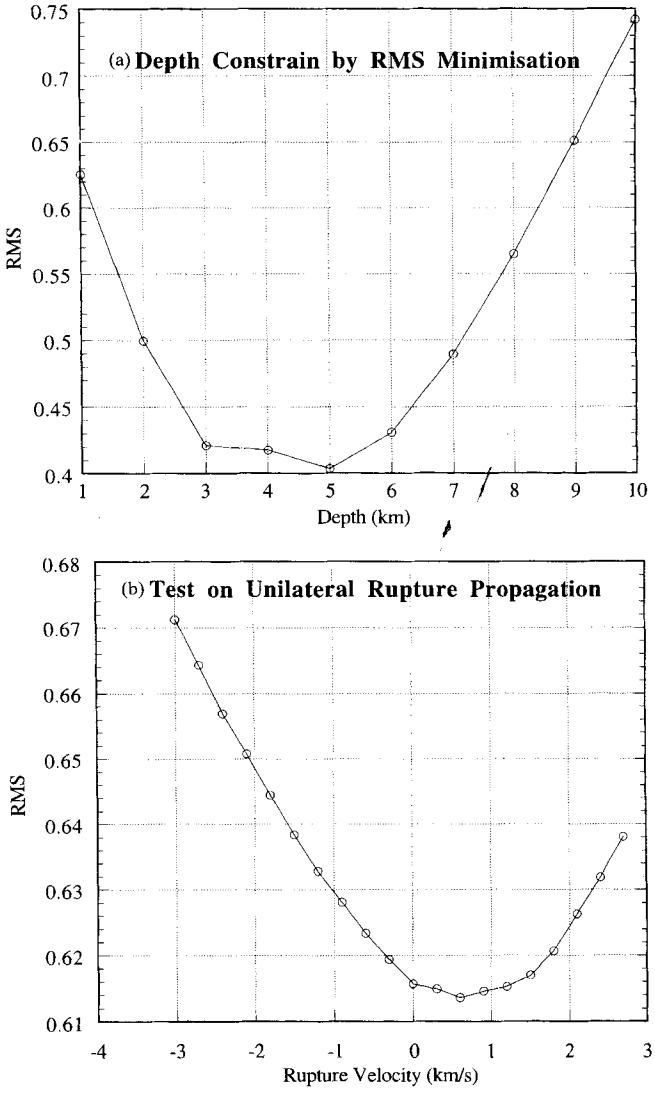

Figure 13. Variation of (normalized) rms values for the point-source inversion solution as a function of (a) depth and (b) rupture velocity. (a) shows that the centroid is around 5 km depth and (b) that there is no clear evidence of unilateral propagation of the rupture.

to stress rotation at the western edge of the fault surface. The fourth group includes the activity to the east of the April 29 aftershock, which follows the basement–cover interface and corresponds to the eastward rupture growth. A clear example of fault growth is given by the 15 June aftershock, whose own aftershock cloud grows even further to the east (Figs 7a and c).

A problem arises in interpreting the June 15 aftershock mechanism since it represents an almost pure E–W shortening. A later event on July 17 shows a similar Harvard CMT solution mechanism (McCormack 1994). The June 15 ($Ms=$ 6.2) event is the largest aftershock in the Racha-Dzhava earthquake sequence, so it cannot be ignored. To explain the mechanism of this aftershock we make only one assumption: the pre-existence of a preferential plane for faulting oriented N–S and dipping to the east, either in the deformed sediments or as the basement–cover interface. The particular orientation of this plane, with respect to that of the local stress tensor, explains the observed mechanism. This statement is immediately verified if we apply the stress tensor obtained

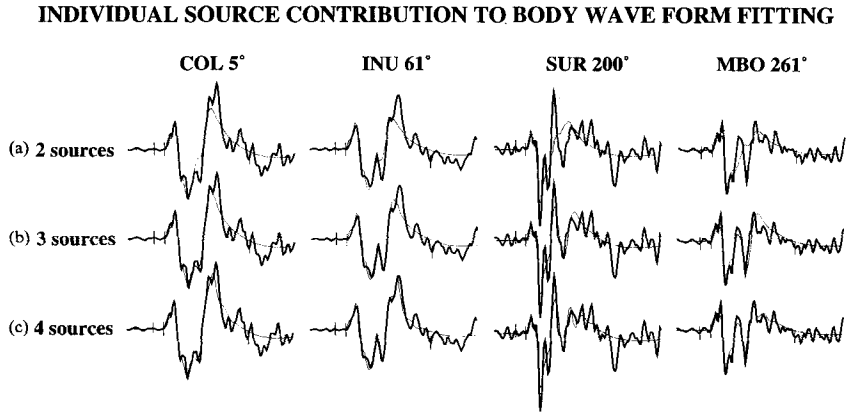

Figure 14. (a) Contribution to the fit of the waveforms for the foreshock at stations COL, INU, SUR and MBO. (b) The same for the third subevent. (c) The same for the fourth subevent. Conventions are as in Fig. 7.

from the aftershock sequence to the fault plane obtained by body-waveform inversion: we obtain the same slip vector as for the event of June 15 (Fig. 17). The previous calculation may be understood in the following way: in the limiting case in which σ_1 is parallel to the fault plane, the slip will be contained in the plane (σ_2, σ_3). The sense of motion will depend on the sign of $(1-R)$, being reverse if $(1-R)>0$, which is the case here (Fig. 8; Rivera & Cisternas 1990). In our case there is a small angle between σ_1 and the azimuth of the fault plane, and a small strike-slip component is observed, but the reverse component is the main one. Thus, it is enough to know the local stress tensor and the geometry of the fault plane in order to understand this mechanism, and it is not necessary to invoke rotations due to the large-scale plate motions or other complex models.

The state of stress (or strain) determines the slip vector on each pre-existing fault. This is why different segments within a large earthquake, or its aftershocks, may exhibit different focal mechanisms with the same stress tensor. Triep *et al.* (1995) present a discussion on the difference in slip-vector direction of their aftershocks III and IV with respect to that of the main shock, and hence conclude that along the strike shortening is also needed.

'Nappe tectonics' as we use the term here consists of a sedimentary cover advancing not only by pushing but also by gravity, and is a relatively common feature in collision zones and at mountain-building fronts. The Zugdidi nappe in the Rioni Basin is a good example. In this sense, their existence has been widely recognised in the Alps, Himalayas, Pyrenees, Caucasus and other mountain chains, but they have rarely been associated with earthquakes. The most important known earthquakes related to nappe tectonics are the 1897 and 1950 Assam earthquakes in the southern Himalayas, both with magnitude estimated around $M=8.7$ (Richter 1958). There is only one other case, to our knowledge, studied in relative detail: the 1985 Nahanni earthquake sequence in the Northwestern Territories, Canada (Wetmiller *et al.* 1988).

Summarizing, all the features mentioned above allow us to propose the following source model. The rupture starts at depth on the interface between the basement and the sedimentary cover, at the northern edge of the nappe, where the underthrusted structure begins to dip steeply, and at the point where the aftershock cloud begins to bifurcate. It then propagates bilaterally towards the southwest, following a shallow-dipping interface until the propagating front cuts upwards into the sediments to end in a blind fault on the southern border of the Racha Range. The whole system is represented qualitatively in the simplified block diagram of Fig. 18, where the sedimentary cover has been removed, and the Dzirula block is seen from the NE and from above.

CONCLUSIONS

Time and space complexity of the source has been resolved by combining complementary information obtained from different disciplines and techniques: the seismicity pattern from the aftershock distribution, the stress tensor determined from first-motion polarities of the aftershocks, and the body-waveform inversion of the teleseismic broad-band records. Tectonic knowledge and observation of the region has allowed us to advance the nappe hypothesis, confirmed later by the seismological data. The rupture started at depth at the northern margin of the nappe, at a point where the aftershock cloud starts branching, and propagated bilaterally. A stress concentration at the extremes of the rupture zone following the main shock is indicated by the increase in aftershock activity at both ends, and by the occurrence of the largest aftershocks there.

The Racha-Dzhava earthquake is one of the first well-documented events to provide evidence of the hidden character of seismicity related to nappe tectonics. It is an example of range-building by cumulative earthquakes on a low-angle blind thrust, which should be added to the case of steep-angle blind faults associated with folding, as observed at Northridge (Stein, King & Lin 1994).

Since no historical earthquakes similar to the 1991 Racha-Dzhava event are known, we may assume that recurrence times may be longer than 1000 yr, which is the period in which historical seismicity is known in the region. Indeed, the Spitak earthquake shows that faults in the Caucasus may have very long recurrence times (Philip *et al.* 1992).

This event, two and a half years after that of Spitak, Armenia, reminds us that large earthquakes are possible, and will certainly occur within the Caucasian ranges in the future. Hence, a re-evaluation of seismic risk for the region on the basis of the new information is necessary.

A clockwise rotation for the stress tensor of 35° is observed with respect to that obtained in the region of the Spitak earthquake. This result confirms the observation obtained

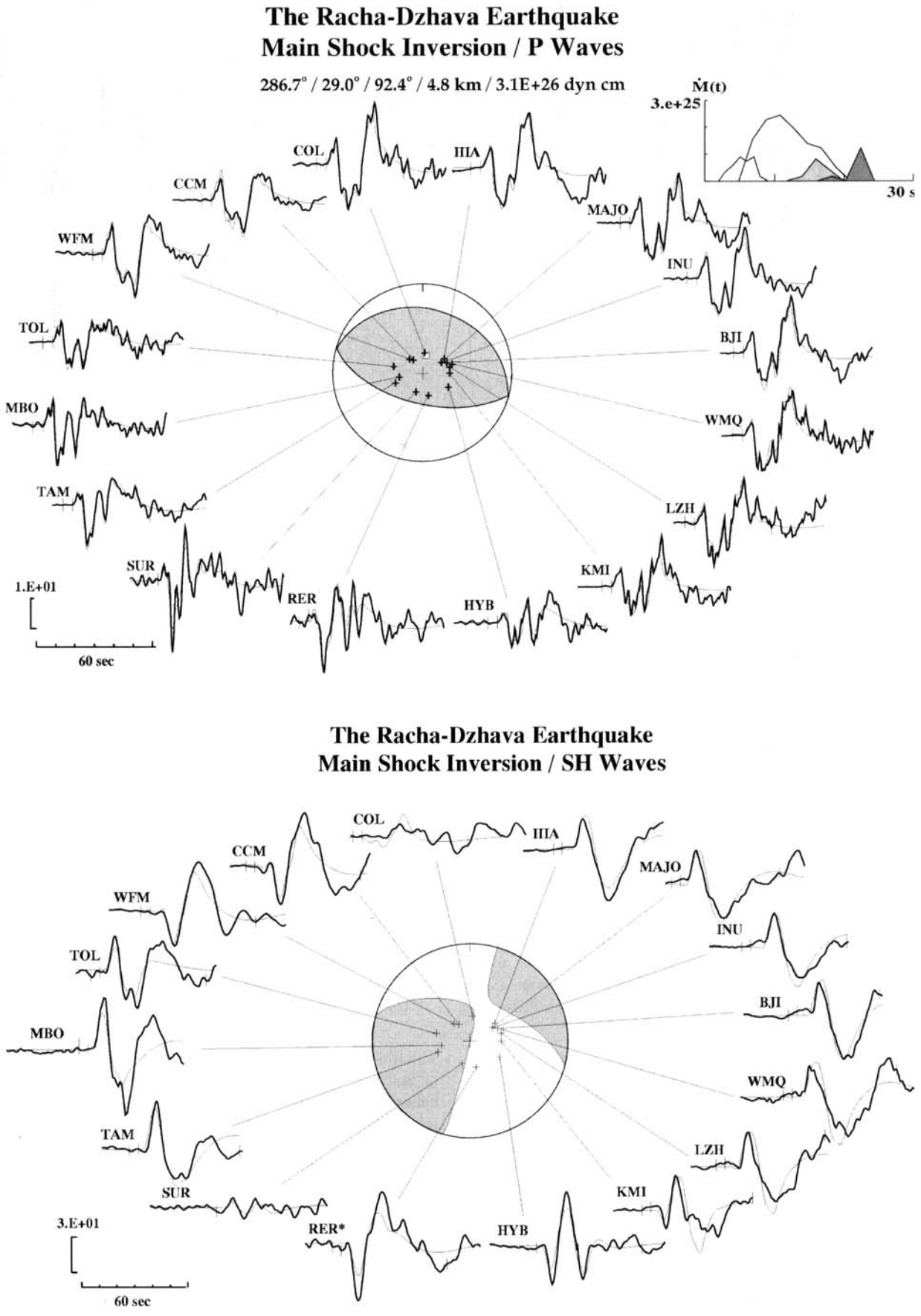

Figure 15. *P*- and *SH*-waveform fitting for the final model, consisting of the four subevents, from inversion of 40 s of signal. The total source time function is shown in the upper left corner, each subevent in a different grey shade. Station RER is not weighted in the inversion of the *SH* waveforms because only one horizontal component was available (E–W). It is shown because *SH* polarization is very close to E–W and the synthetic's polarity is correct.

Table 3. Model and source parameters for the main shock of the Racha-Dzhava earthquake 1991 April 29.

	Horiz. offset (km)	Offset azim. (deg)	Time delay (sec)	Depth (km)	Strike (deg)	Dip (deg)	Slip (deg)	M_o (dyn cm)	Duration (sec)
1st subevent	0.0	0.0	0.0	5.36±0.4	297.6±2.9	48.0±1.5	105.9±1.8	(3.91±0.3) e+25	6
Main Shock	3.1±0.8	122.5±21.3	2.87±0.1	4.81±0.2	286.7±1.3	29.0±0.6	92.4±1.2	(2.27±0.04) e+26	15
2nd subevent	20.7±1.5	309.0±4.3	9.85±0.2	10.3±0.7	300.0±4.1	59.7±1.6	77.6±4.0	(2.18±0.2) e+25	6
3rd subevent	20.0±1.7	280.0±5.6	14.3±0.2	6.5±0.6	26.7±1.9	57.1±3.4	8.4±1.8	(2.67±0.3) e+25	6

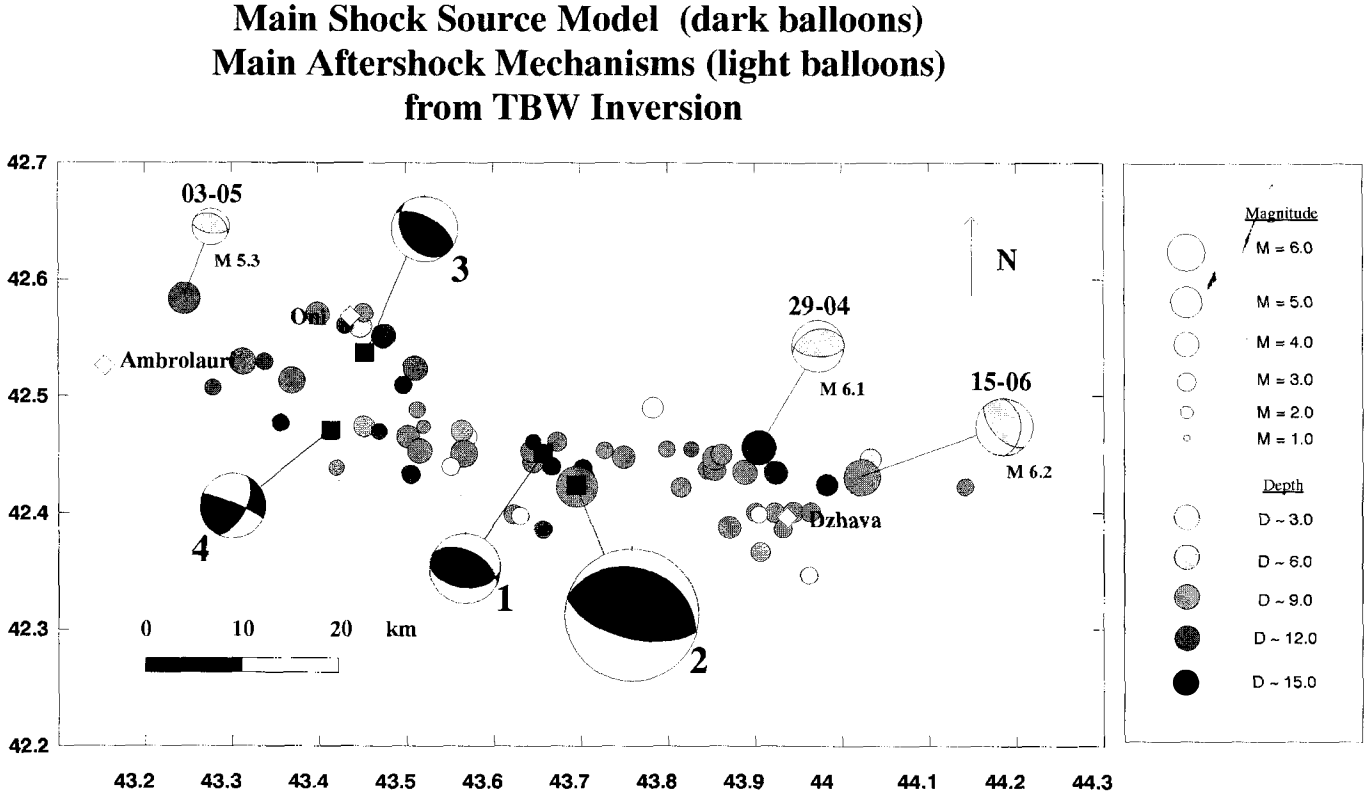

Figure 16. Final model of the main rupture, consisting of the four subevents with focal mechanisms in black. Subevent number 2 releases 72 per cent of the total seismic moment. The radii of the focal spheres are proportional to $(M_o)^{1/3}$. The three strong aftershock solutions are also shown with their dates and with grey focal mechanisms. The epicentres shown are the relocated early aftershocks.

Table 4. Source parameters for the principal aftershocks from teleseismic body-wave inversion.

Aftershock	Latitude (deg)	Longitude (deg)	Depth (km)	Strike (deg)	Dip (deg)	Slip (deg)	M_o (dyn cm)
29°04 M 6.1	42.457	43.905	7.66	251.2	37.5	80.4	1.34 e+25
03°05 M 5.3	42.583	43.245	3.58	290.1	31.5	103.6	4.81 e+24
15°06 M 6.2	42.430	44.023	7.68	342.8	39.7	107.3	1.74 e+25

from microtectonic data (Philip *et al.* 1989), showing that σ_1 rotates when crossing the Borzhomi-Kazbeg fault zone.

The rupture of the main earthquake is in agreement with the regional stress field, but it is strongly controlled by local geology and structural discontinuities, as evidenced by segmentation, the geometry of the different branches and their focal mechanisms. The contrast of mechanical properties between the highly deformable sedimentary cover and the strong crystalline basement is another important factor controlling the rupture surface and the strongest aftershocks.

The aftershock of June 15 shows several remarkable characteristics. First, it illustrates stress concentration at the extremities of the main rupture, with rupture growth to the east. Second, it indicates how local structures determine the way in which a fault may grow. Third, it shows how the orientation of faulting with respect to the axes of stress may affect the behaviour of slip. In our case, the N–S orientation of the fault plane inhibits the role of σ_1, and the slip is subparallel to the plane (σ_1, σ_2). We underline the importance of combining all the independent results in understanding an earthquake sequence. The knowledge of the local stress tensor determined from aftershocks allows us to explain in a simple way the mechanics of faulting of the June 15 aftershock.

ACKNOWLEDGMENTS

We are very grateful to John Nabelek for providing us with the code of his program. The broad-band digital data come

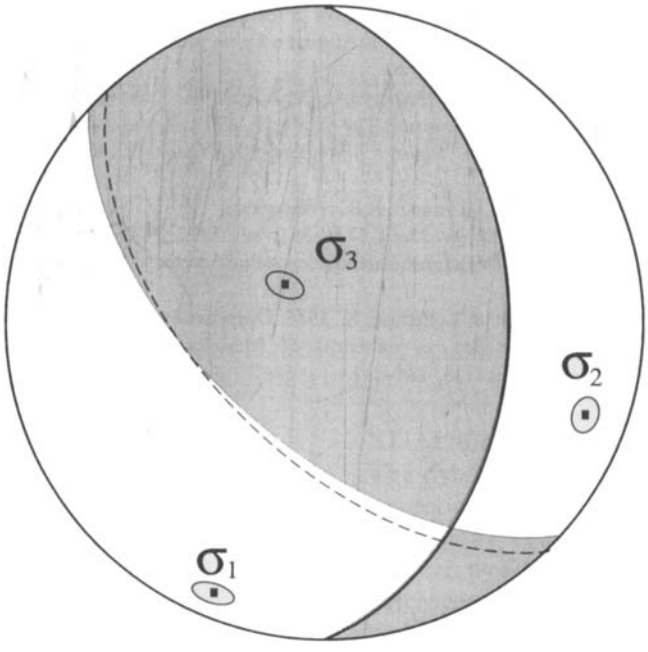

Figure 17. Comparison of the focal mechanism obtained by body-waveform inversion (solid line) with the auxiliary fault plane (dashed line) that is obtained by applying the stress tensor to the N–S-oriented fault plane (dipping east) for the Dzhava aftershock of June 15 (Ms= 6.2). The principal components of the stress tensor are plotted as squares, together with the one standard deviation error ellipses.

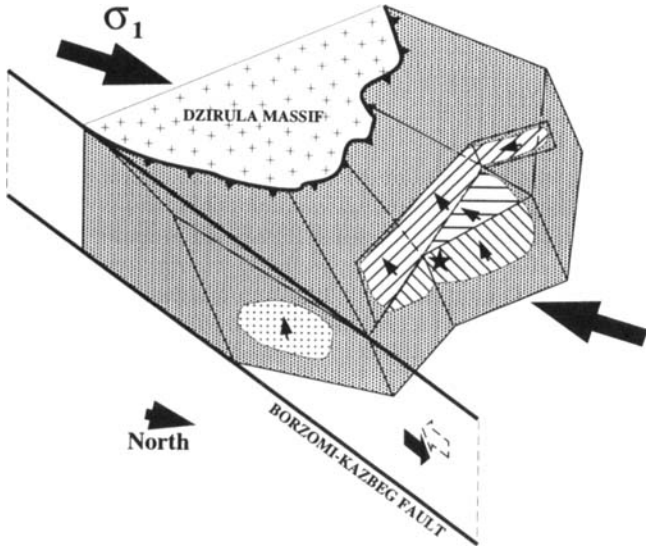

Figure 18. Block diagram showing an interpretation of the main Racha-Dzhava earthquake rupture (hatched surface) and of the June 15 aftershock (dotted area), resulting from a combination of the aftershock results and the source parameters obtained from the body-wave inversion. The hanging block, corresponding to folded Jurassic–Tertiary sediments, has been removed in order to show the ruptured surface (viewed towards the SW). The star indicates the hypocentre of the main shock. Arrows indicate slip directions of the hanging wall.

from the IRIS and GEOSCOPE seismic world network projects. We thank the staff of IRIS and GEOSCOPE for providing us with the digital data. The field expedition was partially supported by the Institut National des Sciences de l'Univers (INSU, France) and by the exchange program between CNRS (France) and the Soviet and Georgian Academies of Sciences.

REFERENCES

Bezzeghoud, M. & Madariaga, R., 1986. Broad band modelling of the Corinth, Greece earthquakes of February and March 1981, *Ann. Geophys.*, **43,** 295–304.

Borisov, B.A., 1982. Strong earthquakes in the eastern Caucasus: interpretation of historical data and analysis of geological situation, *Isvestiya, Earth Physics,* **18,** 726–737.

Borissoff, B. & Rogozhin, E., 1993. The Racha, Georgia, April 29, 1991 earthquake: results of geological investigation, *Russian Acad. Sci., J. Earthquake Prediction,* **1,** 115–125.

Cisternas, A. *et al.*, 1989. The Spitak (Armenia) earthquake of 7 December 1988: field observations, seismology and tectonics, *Nature,* **339,** 645–679.

Dorbath, L., Dorbath, C., Rivera, L., Fuenzalida, A., Cisternas, A., Tatevossian, R., Aptekman, J. & Arefiev, S., 1992. Geometry, segmentation and stress regime of the Spitak (Armenia) earthquake from the analysis of the aftershock sequence, *Geophys. J. Int.*, **108,** 309–328.

Dotduyev, S.I., 1986. Nappe structure of the Greater Caucasus Range, *Geotectonics,* **20,** 420–430.

Fuenzalida, H. *et al.*, 1997. Mechanism of the 1992 Erzincan earthquake and its aftershocks, tectonics of the Erzincan basin and decoupling on the North Anatolian fault, *Geophy. J. Int.*, **129,** 1–28.

Gamkrelidze, I.P., 1986. Geodynamique evolution of the Caucasus and adjacent areas in Alpine time, *Tectonophysics,* **127,** 261–277.

Gorshkov, G.P., 1984. *Regionalaya Seismotektonika Territorii Yuga SSSR: Alpiiskii Poyas,* Nauka, Moscow (in Russian).

Haessler, H., Deschamps, A., Dufumier, H., Fuenzalida, A. & Cisternas, A., 1992. The rupture process of the Armenian earthquake from broad-band teleseismic body wave records, *Geophys. J. Int.*, **109,** 151–161.

I.S.C. Bulletin of the International Seismological Centre, April 1991, 1993. **28**(4), 256.

Jibson, R.W., Prentice, C.S., Borissoff, B.A., Rogozhin, E.A. & Langer, C.J., 1994. Some observations of landslides triggered by the 29 April 1991 Racha earthquake, Republic of Georgia, *Bull. seism. Soc. Am.*, **84,** 963–973.

Kikuchi, M. & Kanamori, H., 1982. Inversion of complex body waves, *Bull. seism. Soc. Am.*, **72,** 491–506.

Kopp, M.L., 1982. Nekatorie voprosi pozdniealpiiskoi geodinamiki yugo-vostochnovo Kavkasa, Talsha i nizhnekurinskoi vpadini, *Problemi geodinamiki Kavkaza,* Nauka, Moscow (in Russian).

Lee, W.H.K. & Lahr, J.C., 1975. HYPO71 (Revised): A computer program for determining hypocentre, magnitude, and first motion pattern of local earthquakes, *USGS Open File Report,* 75–311, Menlo Park, CA.

McCaffrey, R. & Abers, G., 1988. SYN3: A program for inversion of teleseismic body waves forms on microcomputers, *Air Force Geophysical Laboratory Technical Report,* AFGL-TR-88–0099, Hanscom Air Force Base, MA.

McCormack, D., 1994. Local and teleseismic studies of large continental earthquakes, *PhD thesis,* Department of Earth Sciences, University of Cambridge.

Milanovsky, E.E. & Khain, V.E., 1963. Geologicheskoe stroenie Kavkaza. *Izd. M.G.U. in Ocherki Regionalnoi Geologii SSSR,* **8** (in Russian).

Nabelek, J., 1984. Determination of earthquake source parameters from inversion of body waves, *PhD thesis,* MIT, Cambridge, MA.

Nikonov, A.A., 1982. A very powerful earthquake in the Greater Caucasus Mountains, January 14 1668, *Izvestiya, Earth Physics,* **18,** 713–725.

Philip, H., Cisternas, A., Gvishiani, A. & Gorshkov, A., 1989. The

Caucasus: an actual example of the initial stages of continental collision, *Tectonophysics,* **161,** 1–21.

Philip, H., Rogozhin, E., Cisternas, A., Bousquet, J.C., Borisov, B. & Karakhanian, A., 1992. The Armenian earthquake of 1988 December 7: faulting and folding, neotectonics and palaeoseismicity, *Geophys. J. Int.,* **110,** 141–158.

Ramsay, J.G., 1982. Rock ductility and its influence on the development of tectonic structures in mountain belts, in *Mountain Building Processes,* ed. Hsü, K.J., Academic Press, London.

Richter, C.F., 1958. *Elementary Seismology,* Freeman & Co., San Francisco, CA.

Rivera, L. & Cisternas, A., 1990. Stress tensor and fault plane solutions for a population of earthquakes, *Bull. seism. Soc. Am.,* **80,** 600–614.

Stein, R. & Yeats, R., 1989. Les séismes cachés, *Pour la science,* **142,** 30–40.

Stein, R., King, G.C.P. & Lin, J., 1994. Stress triggering of the 1994 m = 6.7 Northridge, California, earthquake by its predecessors, *Science,* **265,** 1432–1435.

Triep, E.G., Abers, G.A. & Lerner-Lam, A.L., 1995. Active thrust front of the Greater Caucasus: The April 29, 1991, Racha earthquake sequence and its tectonic implications, *J. geophys. Res.,* **100,** 4011–4033.

Wetmiller, R.J., Horner, R.B., Hasegawa, H.S., North, R.G., Lamontange, M., Wiechert, D.H. & Evans, S.G., 1988. An analysis of the 1985 Nahanni Earthquakes, *Bull. seism. Soc. Am.,* **78,** 590–616.

Zonenshain, L.P. & LePichon, X., 1986. Deep basins of the Black Sea and Caspian Sea as remnants of Mesozoic back-arc basins, *Tectonophysics,* **123,** 181–211.